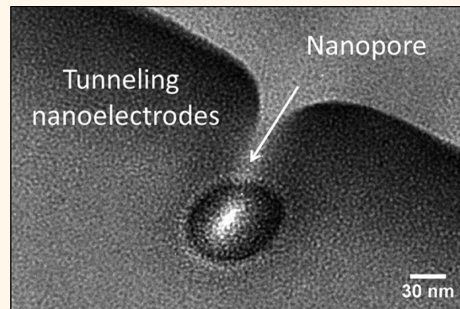


High Precision Fabrication and Positioning of Nanoelectrodes in a Nanopore

Aleksandar P. Ivanov,[†] Kevin J. Freedman,[‡] Min Jun Kim,[§] Tim Albrecht,^{†,*} and Joshua B. Edel^{†,*}

[†]Department of Chemistry, Imperial College London, Exhibition Road, London SW7 2AZ, United Kingdom and [‡]Department of Chemical and Biological Engineering and, [§]Department of Mechanical Engineering and Mechanics, Drexel University, Philadelphia, Pennsylvania 19104, United States

ABSTRACT A simple and versatile method for the direct fabrication of tunneling electrodes with controllable gap distance by using electron-beam-induced deposition (EBID) is presented. We show that tunneling nanogaps smaller than the minimum feature size realizable by conventional EBID can be achieved with a standard scanning electron microscope. These gaps can easily be embedded in nanopores with high accuracy. The controllability of this fabrication method and the nanogap geometry was verified by SEM and TEM imaging. Furthermore, tunneling spectroscopy in a group of solvents with different barrier heights was used to determine the nanogap functionality. Ultimately, the presented fabrication method can be further applied for the fabrication of arrays of nanopore or nanogap electrodes with tunable electrode materials. Additionally, this method can also offer direct fabrication of nanoscale electrode systems with tunable spacing for redox cycling and plasmonic applications, which represents an important step in the development of tunneling nanopore structures and in enhancing the capabilities of nanopore sensors.



KEYWORDS: nanopores · nanopore sequencing · tunneling gaps · label-free detection · single-molecule detection

Nanopores are a remarkable class of single-molecule sensors capable of label-free and rapid detection of biological analytes in solution (e.g., DNA, RNA, proteins). In the past decade, significant advances in solid-state nanopore fabrication have resulted in the ability to precisely tune the nanopore dimensions, membrane material, and surface chemistry, which has resulted in the number of applications continuously growing.^{1–3} However, the detection method employed is largely based on resistive pulse sensing, where analytes are electrokinetically transported through the nanopore and identified by characteristic fluctuations (pulses) in the measured steady-state ionic current. Building on the success of this platform, further developments have led to novel detection strategies, such as tunneling current detection embedded in nanopores.^{4–8} Measuring tunneling current over a steady-state ionic current can offer numerous advantages such as increased sensitivity, spatial resolution, and throughput.^{9,10} By doing so, tunneling technology has the potential to

bring nanopore sensing one step closer to large-scale high-throughput DNA and protein sequence-specific analysis.

One strategy documented in the literature for measuring tunneling currents is by using semiconductor processing techniques to fabricate sub-10 nm junctions either embedded or superimposed on nanopores.^{7,8,11–15} While all of these studies represent technical achievements, the direct and uncomplicated fabrication of tunneling electrodes on a nanopore still remains a formidable challenge. For example, the ability to precisely control the nanogap size and position, necessary for the successful detection of individual molecules in the tunneling gaps aligned to a nanopore, remains a persistent issue. Previously, we demonstrated that it was possible to fabricate tunneling junctions on a nanopore along with proof-of-principle experiments that showed simultaneous detection of DNA translocations using both tunneling and ionic currents in a nanopore platform.⁸ Here, we develop the method and technology further by demonstrating that nanogap

*Address correspondence to t.albrecht@imperial.ac.uk, joshua.edel@imperial.ac.uk.

Received for review December 24, 2013 and accepted January 21, 2014.

Published online January 21, 2014
10.1021/nn406586m

© 2014 American Chemical Society

electrodes aligned to a nanopore can be fabricated with controlled spacing, high precision, and reproducibility by using electron-beam-induced deposition (EBID) in a scanning electron microscope (SEM). Importantly, the nanoelectrodes fabricated with our method have ultrasharp and thin tips (height of only a few nanometers), which is essential for the reliable confinement of analytes in the tunneling nanogap and their accurate detection. The latter results in improvements over other nanogap fabrication techniques (such as break/burn junctions or electrochemical metal deposition), which allow variation of the gap distance but offer less control over the electrode height at the nanogap. This method, in principle, can be performed with a large range of electrode materials (examples include Pt, W, Ge, Ti, Sn, and Cr; cf. ref 16), offering significant flexibility in design and hence application. Furthermore, the method can also be used for the fabrication of nanoscale electrode systems with controllable spacing for redox cycling and plasmonic applications.^{17,18}

We discuss the mechanism of electrode deposition and nanogap formation by lateral broadening and angled deposition and show how electrodes with nanogaps smaller than the minimum feature size realizable by conventional EBID can be easily achieved. We also show that, by varying the electron beam dose during fabrication, we are able to control the electrode dimensions and nanogap size. The fabricated nanogap electrodes have been characterized via electron microscopy, and their functionality has been confirmed via tunneling spectroscopy in different media. All this presents a compelling case for EBID in the fabrication of tunneling nanopore structures for enhancing the capabilities of nanopore sensors.

A unique feature of EBID is that it allows for the fabrication of three-dimensional nanoscale structures directly within a SEM. This is achieved by localized electron-beam-induced decomposition of gas precursors adsorbed to surface of a substrate, a process that can be broadly described as “writing” with the electron beam. In practice, the resolution achievable by EBID is significantly lower than that of the electron beam as secondary electrons (SEs) are generated by the incident (primary) electrons (PEs) in the substrate which affects the deposition process. This undesired lateral broadening of the deposits due to secondary electron emission is often considered one of the prime causes for degradation of the EBID resolution. A detailed discussion on EBID can be found in the critical reviews by Utke *et al.* and van Dorp *et al.*^{16,19} In recent studies, high-resolution single-dot deposits as small as 3 nm (full width at half-maximum) have been demonstrated with a conventional SEM.²⁰ For EBID with scanning transmission electron microscopy (STEM), subnanometer dot deposits have also been achieved.²¹ The shape of the dot deposits is a three-dimensional Gaussian,

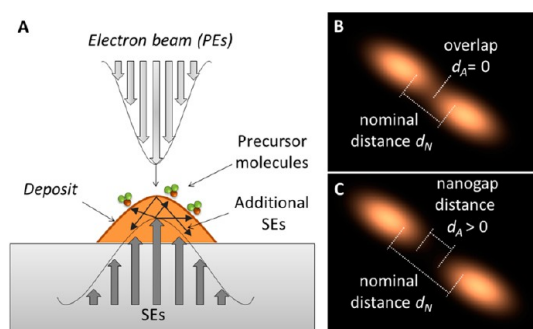


Figure 1. (A) Schematic of the lateral broadening in EBID. SEs are generated in the interaction of the electron beam PEs with the substrate. SEs are generated along the PEs 2 scatter trajectory and have broader distribution than the incident beam. This results in a deposit being broadest at the substrate surface. The deposit can be further broadened at the substrate surface due to additional SE scattering in the newly deposited material. Schematic of Gaussian-shaped deposits illustrating two deposition cases: (B) an overlap and (C) a nanogap formation. The nanowire deposits are separated by a nominal distance, d_N , set in the electron beam writing profile. Due to lateral broadening, the actual gap distance, d_A , between the deposited nanowires is smaller than d_N at the substrate surface.

following the profile of the incident electron beam.^{16,22,23} Furthermore, the lateral size of the EBID deposits considerably exceeds the electron beam spot size and is broadest at the substrate surface.^{20,22} A schematic of the deposition mechanism is shown in Figure 1A.

In comparison to single-dot deposits, the latter broadening is even more pronounced in the deposition of a full nanowire due to higher electron doses required for deposition and additional secondary electron generation in the already deposited structure. This makes the deposition of nanowires with sub-10 nm resolution and, conversely, nanogaps of a few nanometers with a conventional SEM a rather challenging task. However, if the spacing between two EBID features is controlled, it is possible to utilize lateral broadening effects to achieve gap dimensions smaller than a few nanometers between the deposits. This mechanism is illustrated in Figure 1B,C for two single deposits spaced out by a nominal gap distance d_N . An essential property of nanogap fabrication using this strategy is that the height of the nanowire is lowest at the nanogap and gradually increases away from the electrode edge.

In addition to lateral broadening, angled deposition (by tilting the electron beam with respect to the sample) can provide another degree of control of the nanogap and electrode tip shape. The geometrical model illustrated in Figure 1 considers an electron beam perpendicular to the sample (a sample tilt of 0°) that is standard for the EBID process. Tilting the sample with respect to the electron beam during EBID resulted in a decrease of the electrode width in addition to a decrease in the electrode height and gap

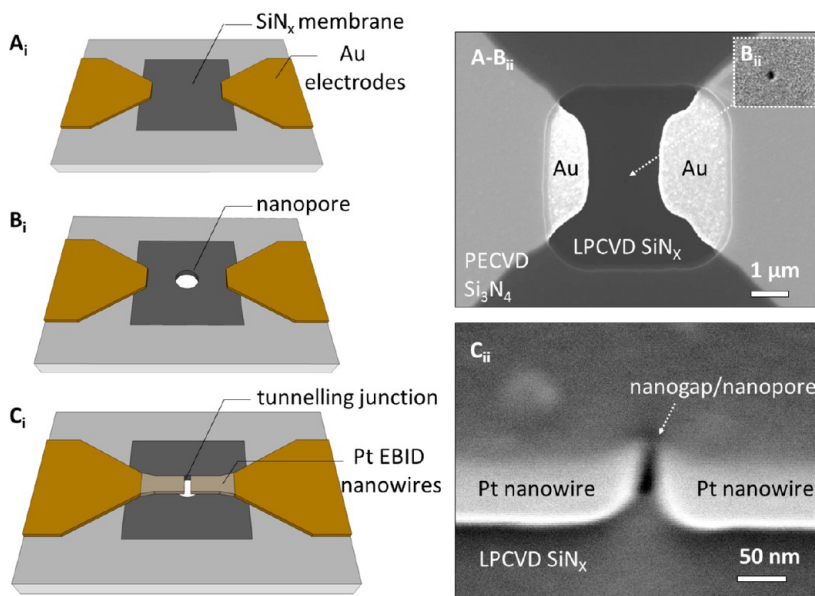


Figure 2. EBID strategy used for the fabrication of tunneling gaps: (A_i) 70 nm thick SiN_x freestanding membrane is fabricated on a chip by standard lithography and combination of dry and wet etching. A pair of Au microelectrodes (2 μ m gap) are fabricated on the membrane and then sealed by 300 μ m PECVD Si₃N₄ layer, leaving only the electrode tips exposed. (B_i) Nanopore is milled in the microelectrode gap by FIB. A SEM of such device is shown on the right; the inset on the top right shows the FIB-milled nanopore. (C_i) Pair of Pt nanowires separated by a nanogap is deposited by EBID precisely over the nanopore. (A–C_{ii}) SEM images corresponding to steps A–C_i. The lateral broadening effect is clearly visible at the nanopore in C_{ii}.

distance. This is attributed partially to lateral broadening, higher secondary electron yield, and extended electron trajectory at the precursor substrate interface during angled deposition.^{19,24} Figure S1 in the Supporting Information shows a reconstructed 3D image from the SEM of a Pt nanogap fabricated by 54° angled EBID. The effects of lateral broadening and nanogap fine-tuning by angled deposition are clearly visible in the V-shaped nanogap on Figure 2C_{ii}. This leads to electrodes with ultrasharp tips, which are particularly important for the fabrication of thin nanogap electrodes, positioned directly at the opening of a nanopore.

RESULTS AND DISCUSSION

We used lateral broadening and angled deposition effects described above for the fabrication of tunneling junctions with EBID by controlling the nominal spacing (d_N) between two EBID nanowires (shown in the schematics in Figure 2A–C_i). The fabrication was done with a standard SEM system (Carl Zeiss Crossbeam 1540). A gaseous precursor (methylcyclopentadienyl-(trimethyl)Pt) was introduced directly in the SEM chamber by a standard gas injection system. For each device, two Pt nanowires (each 1250 nm in length) were deposited in a single line scan and were separated by a gap of a nominal distance d_N that was set in the beam exposure parameters. The substrates were either type 1, SiN_x/Si/SiN_x chips with Au microelectrodes (shown in Figure S2 in the Supporting Information) for tunneling gap characterization, or type 2, SiN_x/Si/SiN_x chips with Au microelectrodes with a nanopore milled in 70 nm freestanding membrane,

for the fabrication of tunneling nanopore devices, as shown in Figure 2A–C_{ii}. All chips and nanopores were fabricated using standard nanofabrication procedures (see Experimental Section for details). To improve the contact between the deposited Pt nanowires and the Au microelectrodes, additional Pt contacts (250 nm \times 500 nm) were deposited by EBID (shown also in S2, Supporting Information).

All EBID processes were performed in electron-limited regime (in the excess of precursor molecules). This allowed us to control the amount of deposited material with the electron dose independently from the number of precursor molecules. For each deposition, the nozzle of the gas injection system was located 300 μ m above the sample. The sample chamber had base pressure of 2×10^{-6} mbar, and deposition was performed when the ambient pressure reached 7×10^{-6} mbar. After deposition, the precursor was pumped out until the pressure returned to base value, then a single scan was made to image the deposited nanowires. This was used for the initial direct and *in situ* assessment of the nanowire properties.

Examples of nanogap electrodes fabricated with controllable spacing are shown in Figure 3 for type 1 devices (SiN_x/Si/SiN_x without a nanopore). It should be noted that we controlled the nominal gap size as an input parameter in the SEM software and established a relationship between the nominal distance and the actual gap distance d_A after deposition, as shown in Figure 1C. The nominal distance d_N was varied systematically from 25 to 70 nm, and nanowire depositions were performed at an electron beam accelerating

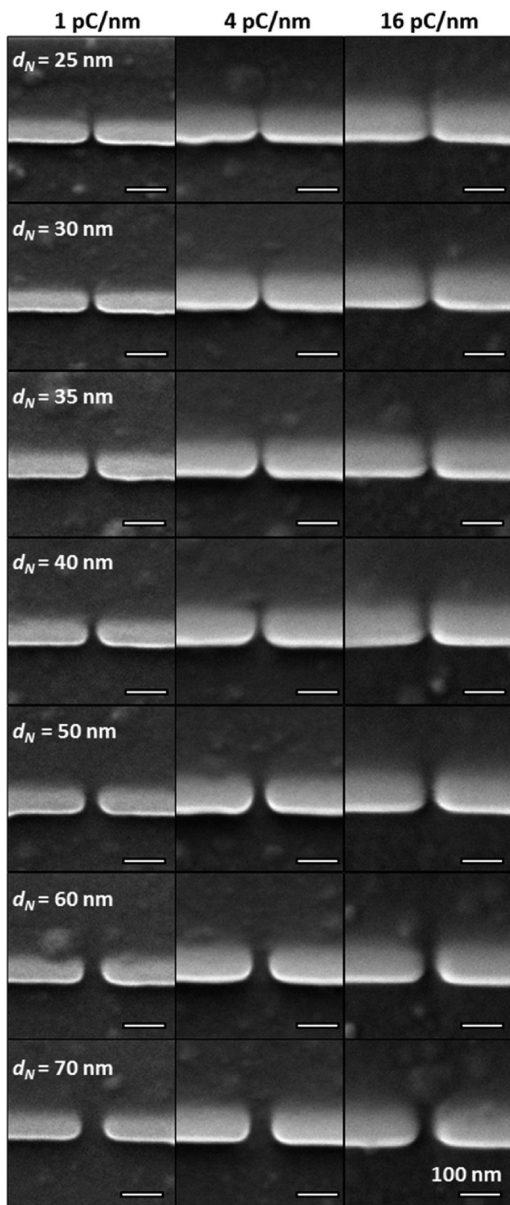


Figure 3. SEM images of nanogaps fabricated with linear doses of 1, 4 and 16 pC/nm (corresponding to aperture diameters of 30, 60, and 120 μm , respectively) for the nominal gap distance ranging from $d_N = 25 \text{ nm}$ to $d_N = 70 \text{ nm}$. Smaller dose settings result in larger nanogaps and wider nanowires at the same nominal distance d_N .

voltage of 30 kV for linear doses of 1, 4, and 16 pC/nm (aperture diameter of 30, 60, and 120 μm , respectively). In all experiments, we observed that a systematic decrease in d_N also resulted in a decrease of the actual gap distance, d_A , as measured by SEM. Larger electron doses are known to increase the width of the deposit,^{16,19} and accordingly, in our depositions, we observed that larger electron doses resulted in wider nanowires. Increasing the dose also resulted in smaller gaps (smaller d_A) between the electrodes at the same nominal distance, which was attributed to higher lateral broadening effect due to the larger number of PEs and generated SEs and more electrons scattering

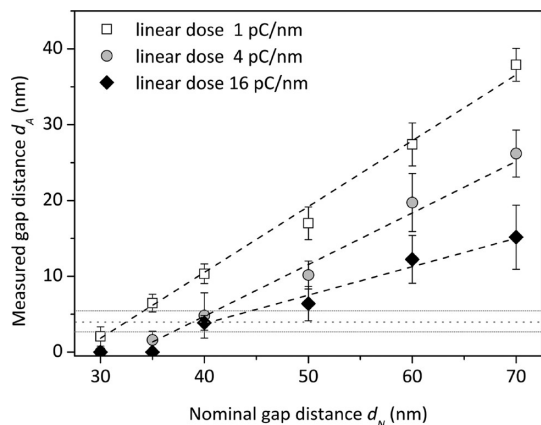


Figure 4. Electrode gap distance d_A as measured by SEM as a function of nominal distance d_N for linear doses of 1, 4, and 16 pC/nm. The SEM images were normalized, and the electrode contours were defined as the threshold above the sum of the average background and three standard deviations. Intercepts at 4 nm (horizontal dotted line with uncertainty interval outlined in gray) were interpolated from the linear fit at $d_N = 32.5 \pm 1.4$, 38.9 ± 1.9 , and $40.6 \pm 2.0 \text{ nm}$ for linear doses of 1, 4, and 16 pC/nm, respectively.

in the wider nanowires. The actual gap distances, d_A , between the deposited nanowires were plotted against their nominal distance (as shown on Figure 4). The nominal distances were significantly larger than the SEM measured gaps due to lateral broadening and scaled linearly with the nominal distance. We observed closing of the gaps for nominal distances smaller than 35 nm for 4 and 16 pC/nm linear doses and for nominal distances smaller than 30 nm for the lowest 1 pC/nm dose.

From the offset between the nominal gap distance and the gap distance d_A , one can assess the amount of lateral broadening in the nanogap region. For two nanowires separated by a gap, the average lateral broadening (LB) can be estimated as

$$\text{LB} = \frac{1}{n} \sum_{i=1}^n \frac{d_{N_i} - d_{A_i}}{2}$$

where d_N is the nominal distance and d_A is the gap distance for n measured gaps. For linear doses of 1, 4, and 16 pC/nm, LB was calculated to be 15.3 ± 1.1 , 19.3 ± 2.1 , and $22.8 \pm 3.9 \text{ nm}$, respectively. As described earlier, lateral broadening arises mainly from electrons escaping from the substrate surface and the newly formed deposit. For all doses, the LB was consistent with the maximum electron escape length T . The mean escape depth of SEs in silicon nitride (the top layer of the $\text{SiN}_x/\text{Si}/\text{SiN}_x$ devices used) is estimated to be $\Lambda = 4.5 \text{ nm}$.²⁵ The maximum electron escape length T of secondary electron is approximately 5Λ or 22.5 nm for silicon nitride. During deposition, the electrons with maximum escape length can determine the region where the gap is shortest, which in turn governs the tunneling current measured across the gap. Since both nanowires have lateral broadening, this condition for a

nanogap is $d_N \sim 2T$ (T for each deposited nanowire) or approximately 45 nm.

In general, under ideal conditions (low noise and long detection time), a junction with a gap size of approximately 4 nm or smaller is required for the detection of single molecules positioned in the tunneling gap⁹ (in less favorable experimental conditions, d_A is required to be much smaller). Figure 4 can be used for initial assessment of the nominal distance and the dose conditions that are suitable for the fabrication of nanogap devices with gap distance in the interval between $d_A > 0$ nm and $d_A \leq 4$ nm. Intercepts at $d_A = 4$ nm (approximate onset for measurable tunneling current, dashed line in Figure 4) were interpolated from the linear fits at $d_N = 32.5 \pm 1.4$, 38.9 ± 1.9 , and 40.6 ± 2.0 nm for linear doses of 1, 4, and 16 pC/nm, respectively. Based on the SEM measurements, nanowires separated by gaps with nominal distance between 35 and 45 nm are probably best suited for the fabrication of tunneling nanogaps.

For small gaps, the SEM measurements have a large relative error, and although SEM was used for the estimation gap sizes, the functionality of the gaps can only be verified by tunneling spectroscopy. We performed I – V tunneling spectroscopy of nanogap/nanopore devices in a group of solvents with different tunneling barriers (air, isopropyl alcohol, and dimethylsulfoxide (DMSO)). For each junction, multiple chronoamperometric curves were measured (ranging from -0.6 to 0.6 V with a 0.015 V step and 0.2 s step duration) under Ar atmosphere.

For gaps with d_N smaller than 40 nm, we observed currents higher than 100 nA (at 0.6 V bias) that overloaded our current amplifier, suggesting that these junctions were either very small or closed. We also observed currents higher than 100 nA (at 0.6 V bias) for control devices with a single nanowire (without a gap, $d_N = 0$; cf. Supporting Information, Figure S3). When d_N is higher than 70 nm, the measured currents were too small and indistinguishable from background current noise (<20 pA peak-to-peak). For devices fabricated with d_N ranging from 40 to 70 nm, however, nonlinear I – V curves were measured with current magnitude increasing systematically with decreasing d_N , as anticipated for functional tunneling junctions (Figure 5A). To confirm that functional tunneling junctions were fabricated, we performed I – V spectroscopy in different solvents (*i.e.*, with different barrier heights). Differences in the tunneling current are expected for a nanogap immersed in solvents with different barrier heights. Tunneling barriers for IPA and DMSO have been reported to be $\phi_{B,IPA} = 1.68$ eV and $\phi_{B,DMSO} = 2.12$ eV.²⁶ The barrier height for air has been reported to range from 0.7 to 4.7 eV depending on the local environment. In nanogaps with d_N ranging from 40 to 70 nm, we observed current magnitudes in the order $I_{IPA} > I_{DMSO} > I_{air}$, in agreement with $\phi_{B,IPA} < \phi_{B,DMSO} < \phi_{B,air}$.

Importantly, this trend was preserved when randomizing the order in which the solvents were measured and is in good agreement with results that have been previously reported.⁸

Fitting the current–voltage curves in Figure 5A using eq 1 is possible based on three fitting parameters (barrier height ϕ , distance d , tunneling active area A) but complicated by the fact that they are not mutually independent. An assumption is usually made with regards to A ; however, the actual value is difficult to determine experimentally in an independent way. One way to avoid this difficulty is to use the ratio of the tunneling conductance for different tunneling media 1 and 2, that is, with different tunneling barriers $\phi_{B,1}$ and $\phi_{B,2}$, respectively. Assuming that the medium has a negligible effect on A , this factor then cancels out in the conductance ratio. We illustrate this approach for measurements performed in air and in DMSO as an example below.

Following the Simmons model for a rectangular barrier,²⁷ the tunneling current I_t can be written as

$$I_t = A \cdot \frac{e}{4\pi^2\hbar \cdot d^2} \cdot \left\{ \left(\phi_B - \frac{e \cdot V_{bias}}{2} \right) \cdot \exp \left(-\frac{2\sqrt{2m_e}}{\hbar} \cdot \left(\phi_B - \frac{e \cdot V_{bias}}{2} \right)^{1/2} \cdot d \right) - \left(\phi_B + \frac{e \cdot V_{bias}}{2} \right) \cdot \exp \left(-\frac{2\sqrt{2m_e}}{\hbar} \cdot \left(\phi_B + \frac{e \cdot V_{bias}}{2} \right)^{1/2} \cdot d \right) \right\} \quad (1)$$

where e is the elemental charge, d the tunneling distance, ϕ_B the tunneling barrier, V_{bias} the bias voltage between the two tunneling electrodes, and m_e the electron mass (taken as the mass of a free electron here).

The tunneling conductance is the derivative of I_t with respect to V_{bias} , in the limit of $V_{bias} \rightarrow 0$. This yields

$$G_t = \frac{1}{4} \frac{e^2 A}{\hbar^2 \pi^2 \cdot d^2} \cdot \frac{\sqrt{2m_e \phi_B} \cdot d - \hbar}{\exp \left(-\frac{2\sqrt{2m_e \phi_B} \cdot d}{\hbar} \right)} \quad (2)$$

The conductance ratio for different media with tunneling barriers $\phi_{B,1}$ and $\phi_{B,2}$ is then

$$G_{rat} = \frac{G_{t,1}}{G_{t,2}} = \frac{\sqrt{2m_e \phi_{B,1}} \cdot d - \hbar}{\sqrt{2m_e \phi_{B,2}} \cdot d - \hbar} \cdot \exp \left(-\frac{2\sqrt{2m_e} \cdot (\phi_{B,1}^{1/2} - \phi_{B,2}^{1/2}) \cdot d}{\hbar} \right) \quad (3)$$

Hence G_{rat} is only dependent on d as well as $\phi_{B,1}$ and $\phi_{B,2}$. If the latter are known from other sources, such as from STM-based tunneling current–distance spectroscopy data, then d may be determined.

In our experiments, the nanogap conductance G_t of each device was measured in the low-bias regime (-0.2 V; 0.2 V), where the I – V curves were linear. Figure 5B shows the average nanogap conductance

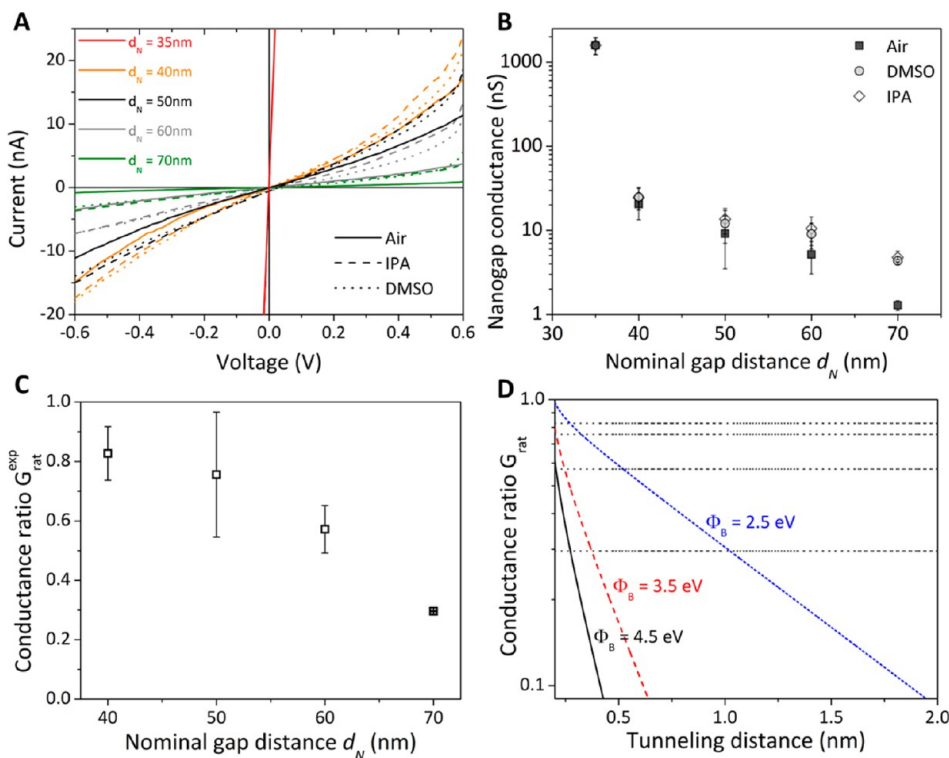


Figure 5. (A) Tunneling spectroscopy performed in air (solid), IPA (dashed), and DMSO (dotted) for devices with nanogaps fabricated with different nominal distance settings ($d_N = 35\text{--}70\text{ nm}$) linear doses of 16 pC/nm . (B) Average nanogap conductance G_t measured for a group of 15 devices (3 devices for each d_N from 35 to 70 nm) each measured in air, IPA, and DMSO. All devices were fabricated with a linear dose of 16 pC/nm . The nanogap conductance of each device was measured in a low bias (-0.2 V ; 0.2 V) regime, where the I - V curves showed linear (ohmic) characteristics. (C) Experimental tunneling conductance ratio, $G_{rat}^{exp} = G_{air}/G_{DMSO}$, as a function of nominal gap distance. (D) Tunneling conductance ratio, $G_{rat} = G_{air}/G_{DMSO}$, as a function of distance for different barrier heights. Horizontal (dotted) lines: experimental G_{rat}^{exp} simulations based on eq 3.

measured for a group of 15 devices (3 devices for each d_N setting) each measured in air, IPA, and DMSO. All of the devices were fabricated with a linear dose of 16 pC/nm . In all cases, the nanogap conductance decreased with increasing nominal distance. For devices with $d_N < 40\text{ nm}$, the observed conductance is high and independent of solvent. These devices appear to be short-circuited (*i.e.*, G_t is similar to a continuous nanowire). The conductance ratio for different media according to eq 3 was close to 1. Remarkably, increasing the nominal distance by just 5 nm to $d_N = 40\text{ nm}$ resulted in a 40-fold lower nanogap conductance. For devices with $d_N \geq 40\text{ nm}$, G_t decreases with increasing d_N and varies with the solvent used, in agreement with the expected change in G_t (*i.e.*, $G_{t,IPA} > G_{t,DMSO} > G_{t,air}$ with $\phi_{B,IPA} < \phi_{B,DMSO} < \phi_{B,air}$). This indicates the onset of the tunneling regime. Importantly, the observed onset of the tunneling regime for gaps with $d_N \geq 40\text{ nm}$ is in very good agreement with the lateral broadening values for a gap of $2LB$ (LB for each nanowire in the gap) or $45.6 \pm 7.8\text{ nm}$ (for a linear dose of 16 pC/nm).

On the basis of known values for the tunneling barriers, we now use eq 3 to estimate the actual gap distance d . As expected from the correlation between d_N and d , G_{rat} changes with d_N , as shown in Figure 5C. The barrier heights reported for air in comparable

systems vary significantly, hence air barrier heights were chosen ranging from the maximum value reported for comparable systems ($\sim 4.5\text{ eV}$) to a value close to the barrier reported for DMSO (2.12 eV). Combining these from the experimentally measured G_{rat} , we obtained tunneling gap distances ranging from 0.2 (for 4.5 eV) to 1 nm (for 2.5 eV) (Figure 5D). It is currently not clear whether the actual gap size is indeed that small or whether the small values are at least in part due to shortcomings in the underlying model. However, the general approach of analyzing tunneling data in this way still has considerable merit. The existence of parasitic current paths cannot be ruled out at this stage, even though they are not easily reconciled with the observed medium dependence of the tunneling current. Hence, their relative contribution is likely to be small.

Nonlinear current–voltage characteristics of single Pt nanowires fabricated by EBID have been previously reported by Rotkina *et al.* and were attributed to single-electron tunneling *via* Pt nanocrystals in the deposit.²⁸ This mechanism does not however explain the strong current dependence on nominal distance and barrier height of the environment observed in our experiments. To distinguish from this case, we applied the above method for the deposition of nanogap nanowire electrodes that were aligned to a nanopore milled in a

70 nm thick freestanding SiN_x membrane in $\text{SiN}_x/\text{Si}/\text{SiN}_x$ chips (type 2). Suspending the electrodes over a larger nanopore also prevents gap contamination by single Pt crystallites that could potentially be deposited in the EBID process due to random electron scattering in the gap. The nanogap is directly positioned over the nanopore, and there is no membrane substrate to support the growth of such Pt nanocrystallites. We confirmed the latter as well as the gap geometry by high-resolution imaging with TEM (Figure 6A).

These nanogap/nanopore devices were characterized by tunneling spectroscopy. We observed systematic

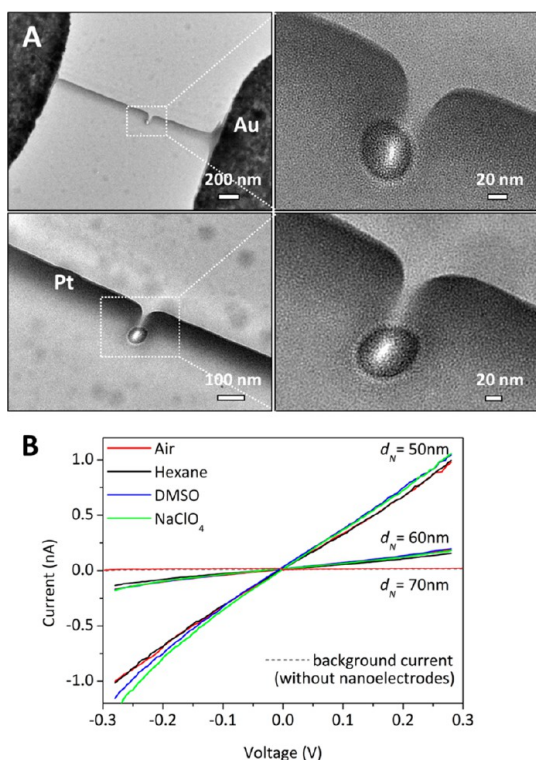


Figure 6. (A) TEM images of nanogap/nanopore devices fabricated by EBID (left) and higher magnification of the nanogap/nanopore. (B) Tunnelling spectroscopy performed in air (red), *n*-hexane (black), DMSO (blue), and 0.1 M NaClO_4 (green) for devices with nanogap/nanopores fabricated with different nominal distance settings (from $d_N = 50$ to $d_N = 70$ nm); the linear dose is 16 pC/nm. Dashed line shows the background current (without nanoelectrode deposition).

variation in the current magnitude with decreasing d_N . For the same d_N values, the current measured in type 2 devices had smaller magnitude (Figure 6B) compared to measurements of type 1 (Figure 5A) for the same linear dose of 16 pC/nm. This relative decrease in current magnitude is expected, as type 2 devices were fabricated on a freestanding 70 nm membrane, while the devices without a nanopore had an additional Si supporting substrate with a thickness of 300 μm . All nanogaps were fabricated with electron beam energy of 30 keV, and the majority of PEs had sufficiently high energy to penetrate through the 70 nm SiN_x membrane (at 2 keV, the electron penetration depth is approximately 70 nm). Membrane substrates display less scattering than bulk, and at higher energy, the electrons spread less along their incident trajectory and generate secondary electrons with smaller exit area. In membrane substrates, there are fewer secondary electrons generated and less material is deposited, which results the larger gaps in nanogap/nanopore devices under the same fabrication conditions.

Importantly, although the current magnitude for the same d_N was lower in type 2 devices, tunnelling spectroscopy measurements in a range of solvents (hexane, DMSO, and 0.1 M NaClO_4 and in air) showed reproducible variation in the $I-V$ curves, depending on the solvent barrier heights, similar to the type 1 devices. Barrier heights of 3.46, 2.12, and 0.93 eV have been reported, respectively, for hexane, DMSO, and water.²⁶ Also, a strong correlation was observed between the measured current and solvent barrier height ($I_{\text{NaClO}_4} > I_{\text{DMSO}} > I_{\text{hexane}}$) in agreement with $\phi_{\text{B,NaClO}_4} < \phi_{\text{B,DMSO}} < \phi_{\text{B,hexane}}$. Similar to the measurements of nanogaps in type 1 devices, tunnelling conductance ratios $G_{\text{rat}} = G_{\text{air}}/G_{\text{DMSO}}$ were extracted. For the smallest nominal distance settings in these measurements ($d_N = 50$ nm), G_{rat} as high as 0.9 was measured, yielding a gap size of less than 1 nm. Again, in the low-bias regime, G_t decreases with increasing d_N and varies with the solvent used, in agreement with the expected change in G_t (i.e., $G_{t,\text{NaClO}_4} > G_{t,\text{DMSO}} > G_{t,\text{hexane}}$ with $\phi_{\text{B,NaClO}_4} < \phi_{\text{B,DMSO}} < \phi_{\text{B,air}}$). This indicates that the tunnelling junctions in the nanogap/nanopore devices were

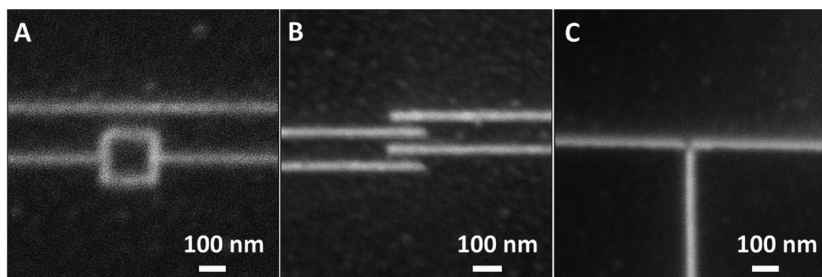


Figure 7. SEM of complex nanoscale electrode structures fabricated via EBID that could be potentially used in single-molecule trapping and sensing applications, for example, a (negative) dielectrophoretic trap (A),^{30,31} interdigitated and gated nanoelectrode junctions (B,C).

functional and demonstrates the flexibility of the method for nanoelectrode fabrication in devices with different membrane thickness or supporting substrate structure.

Finally, it is noteworthy that, for the fabrication of nanogap/nanopore devices, the alignment process is controlled by the SEM, and it was possible to achieve nanogap/nanopore alignment with resolution comparable to that of conventional EBID (on the order of 10 nm). Importantly, the deposition of nanogap nanowire electrodes over the nanopore resulted in simultaneous reduction of the nanopore opening diameter. This allowed for 30–40 nm FIB milled pores to be tuned down to sub-10 nm effective diameters. Such nanopore dimensions are typically achieved by more complex and lower-throughput instruments such as (S)TEM or helium ion beam.^{2,29}

CONCLUSIONS

Here we show how EBID lateral broadening can be used for the fabrication of complex nanoelectrode structures, namely, high-resolution tunneling junctions aligned with a nanopore, by EBID using a standard SEM. This allows for the fabrication of sharp electrodes with low height, which is particularly important for analyte confinement and accurate nanopore/nanoelectrode

detection. To our knowledge, this work is the first example of using lateral broadening deposition in the controlled fabrication of high-resolution nanogap/nanopore structures. The controllability of this fabrication method and the nanogap geometry was confirmed by SEM and TEM imaging and tunneling spectroscopy. We also confirmed the tunneling functionality of both nanogap and nanogap/nanopore structures in a group of solvents with different tunneling barrier heights.

The presented method can be further used for the fabrication of nanogap electrodes with tunable surface chemistry, due to the wide choice of available EBID precursors. In addition, it is possible to readily apply the method for the fabrication of nanogap/nanopore arrays (examples shown in Figure S4, Supporting Information). Moreover, this technique can offer a promising route for direct deposition of complex nanoscale electrode structures for applications beyond tunneling detection, for example, in plasmonics and dielectrophoretic trapping (Figure 7).

Above all, this method provides easily accessible fabrication of nanogap/nanopore platforms that combine the advantages of confinement in nanopores of individual nucleic acids and other biologically relevant analytes and highly sensitive, high-throughput tunneling-based detection.

EXPERIMENTAL SECTION

Device Fabrication. The device microfabrication protocol is illustrated in Figure S5 in the Supporting Information. Briefly, SiN_x was deposited by low-pressure chemical vapor deposition (LPCVD) on both faces of a bare silicon (100) wafer to a thickness of 70 nm. Microelectrodes with a 1.5–2.0 μm gap (50 nm thick gold with 10 nm chromium adhesion layer) were fabricated by conventional optical lithography on the front face of the wafer. These devices were labeled type 1, and representative SEM images are shown in Figure S2.

For $\text{SiN}_x/\text{Si}/\text{SiN}_x$ devices with 70 nm SiN_x freestanding membrane (type 2), reactive ion etching was used to etch a 474 $\mu\text{m} \times 474 \mu\text{m}$ window in the silicon nitride film on one side of the wafer (back side). An additional 300 nm thick layer of silicon nitride was deposited by plasma-enhanced chemical vapor deposition (PECVD). Windows (5 $\mu\text{m} \times 5 \mu\text{m}$) centered at the microelectrode tips were opened in the PECVD Si_3N_4 layer. A window in the LPCVD nitride on the back face of the wafer was opened by reactive ion etching, followed by wet etch of the silicon in KOH solution, resulting in a 70 nm thick freestanding SiN_x membrane (45 $\mu\text{m} \times 45 \mu\text{m}$) aligned to the microelectrodes (Figure 2A-Bii). Oxygen plasma cleaning of all devices was performed before milling and/or deposition to minimize hydrocarbon contamination.

Nanopore Milling. Nanopores were milled using a focused ion beam (FIB) with a Zeiss CrossBeam 1540XB. Nanopores with 30–40 nm diameters were milled in $\text{SiN}_x/\text{Si}/\text{SiN}_x$ devices with 70 nm SiN_x freestanding membrane, in a single spot exposure at 1 pA, 30 kV for 2–2.5 s. The nanopore dimensions were confirmed by SEM imaging.

TEM Imaging. The TEM used for all nanogap imaging was a JEOL JEM 2100 equipped with a LaB_6 electron source. The nanogap/nanopore devices ($\text{SiN}_x/\text{Si}/\text{SiN}_x$ devices with 70 nm SiN_x freestanding membrane) were loaded into the TEM by placing them into a custom-built holder that was subsequently attached to the TEM goniometer. The accelerating voltage used

throughout was 200 kV since lower accelerating voltages yielded a less intense image due to reduced electron transmission. All images were taken with no tilting of the specimen stage.

Conflict of Interest: The authors declare no competing financial interest.

Acknowledgment. J.B.E. has been funded in part by an ERC starting investigator grant and a Leverhulme Trust grant.

Supporting Information Available: Additional figures and experimental details as described in text. This material is available free of charge via the Internet at <http://pubs.acs.org>.

REFERENCES AND NOTES

- Dekker, C. Solid-State Nanopores. *Nat. Nanotechnol.* **2007**, *2*, 209–215.
- Miles, B. N.; Ivanov, A. P.; Wilson, K. A.; Dogan, F.; Japprung, D.; Edel, J. B. Single Molecule Sensing with Solid-State Nanopores: Novel Materials, Methods, and Applications. *Chem. Soc. Rev.* **2013**, *42*, 15–28.
- Wanunu, M. Nanopores: A Journey towards DNA Sequencing. *Phys. Life Rev.* **2012**, *9*, 125–158.
- Lagerqvist, J.; Zwolak, M.; Di Ventra, M. Fast DNA Sequencing via Transverse Electronic Transport. *Nano Lett.* **2006**, *6*, 779–782.
- Zwolak, M.; Di Ventra, M. Electronic Signature of DNA Nucleotides via Transverse Transport. *Nano Lett.* **2005**, *5*, 421–424.
- Liang, X. G.; Chou, S. Y. Nanogap Detector Inside Nanofluidic Channel for Fast Real-Time Label-Free DNA Analysis. *Nano Lett.* **2008**, *8*, 1472–1476.
- Taniguchi, M.; Tsutsui, M.; Yokota, K.; Kawai, T. Identifying Single Nucleotides by Tunnelling Current. *Nat. Nanotechnol.* **2010**, *5*, 286–290.
- Ivanov, A. P.; Instuli, E.; McGilvery, C. M.; Baldwin, G.; McComb, D. W.; Albrecht, T.; Edel, J. B. DNA Tunneling

Detector Embedded in a Nanopore. *Nano Lett.* **2011**, *11*, 279–285.

9. Lindsay, S.; He, J.; Sankey, O.; Hapala, P.; Jelinek, P.; Zhang, P. M.; Chang, S. A.; Huang, S. O. Recognition Tunneling. *Nanotechnology* **2010**, *21*, 262001.

10. Albrecht, T. Electrochemical Tunnelling Sensors and Their Potential Applications. *Nat. Commun.* **2012**, *3*, 829.

11. Spinney, P. S.; Collins, S. D.; Howitt, D. G.; Smith, R. L. Fabrication and Characterization of a Solid-State Nanopore with Self-Aligned Carbon Nanoelectrodes for Molecular Detection. *Nanotechnology* **2012**, *23*, 135501.

12. Tsutsui, M.; Rahong, S.; Iizumi, Y.; Okazaki, T.; Taniguchi, M.; Kawai, T. Single-Molecule Sensing Electrode Embedded In-Plane Nanopore. *Sci. Rep.* **2011**, *1*, 46.

13. Healy, K.; Ray, V.; Willis, L. J.; Peterman, N.; Bartel, J.; Drndić, M. Fabrication and Characterization of Nanopores with Insulated Transverse Nanoelectrodes for DNA Sensing in Salt Solution. *Electrophoresis* **2012**, *33*, 3488–3496.

14. Fischbein, M. D.; Drndić, M. Sub-10 nm Device Fabrication in a Transmission Electron Microscope. *Nano Lett.* **2007**, *7*, 1329–1337.

15. Jiang, Z. J.; Mihovilovic, M.; Chan, J.; Stein, D. Fabrication of Nanopores with Embedded Annular Electrodes and Transverse Carbon Nanotube Electrodes. *J. Phys.: Condens. Matter* **2010**, *22*, 454114.

16. Utke, I.; Hoffmann, P.; Melngailis, J. Gas-Assisted Focused Electron Beam and Ion Beam Processing and Fabrication. *J. Vac. Sci. Technol., B* **2008**, *26*, 1197–1276.

17. Jonsson, M. P.; Dekker, C. Plasmonic Nanopore for Electrical Profiling of Optical Intensity Landscapes. *Nano Lett.* **2013**, *13*, 1029–1033.

18. Cecchini, M. P.; Wiener, A.; Turek, V. A.; Chon, H.; Lee, S.; Ivanov, A. P.; McComb, D. W.; Choo, J.; Albrecht, T.; Maier, S. A.; Edel, J. B. Rapid Ultrasensitive Single Particle Surface-Enhanced Raman Spectroscopy Using Metallic Nanopores. *Nano Lett.* **2013**, *13*, 4602–4609.

19. van Dorp, W. F.; Hagen, C. W. A Critical Literature Review of Focused Electron Beam Induced Deposition. *J. Appl. Phys.* **2008**, *104*, 081301.

20. van Kouwen, L.; Botman, A.; Hagen, C. W. Focused Electron-Beam-Induced Deposition of 3 nm Dots in a Scanning Electron Microscope. *Nano Lett.* **2009**, *9*, 2149–2152.

21. van Dorp, W. F.; Zhang, X. Y.; Feringa, B. L.; Hansen, T. W.; Wagner, J. B.; Hosson, J. T. M. Molecule-by-Molecule Writing Using a Focused Electron Beam. *ACS Nano* **2012**, *6*, 10076–10081.

22. Kohlmannvomplaten, K. T.; Chlebek, J.; Weiss, M.; Reimer, K.; Oertel, H.; Brunger, W. H. Resolution Limits in Electron-Beam-Induced Tungsten Deposition. *J. Vac. Sci. Technol., B* **1993**, *11*, 2219–2223.

23. Silvis-Cividjian, N.; Hagen, C. W.; Leunissen, L. H. A.; Kruit, P. The Role of Secondary Electrons in Electron-Beam-Induced-Deposition Spatial Resolution. *Microelectron. Eng.* **2002**, *61–62*, 693–699.

24. Kunz, R. R.; Mayer, T. M. Catalytic Growth-Rate Enhancement of Electron-Beam Deposited Iron Films. *Appl. Phys. Lett.* **1987**, *50*, 962–964.

25. Joy, D. C. *Monte Carlo Modeling for Electron Microscopy and Microanalysis*; Oxford University Press: New York, 1995; p viii, 216.

26. Prokopuk, N.; Son, K. A.; Waltz, C. Electron Tunneling through Fluid Solvents. *J. Phys. Chem. C* **2007**, *111*, 6533–6537.

27. Simmons, J. G. Generalized Formula for the Electric Tunnel Effect between Similar Electrodes Separated by a Thin Insulating Film. *J. Appl. Phys.* **1963**, *34*, 1793–1803.

28. Rotkina, L.; Lin, J. F.; Bird, J. P. Nonlinear Current–Voltage Characteristics of Pt Nanowires and Nanowire Transistors Fabricated by Electron-Beam Deposition. *Appl. Phys. Lett.* **2003**, *83*, 4426–4428.

29. Yang, J. J.; Ferranti, D. C.; Stern, L. A.; Sanford, C. A.; Huang, J.; Ren, Z.; Qin, L. C.; Hall, A. R. Rapid and Precise Scanning Helium Ion Microscope Milling of Solid-State Nanopores for Biomolecule Detection. *Nanotechnology* **2011**, *22*, 285310.

30. Rosenthal, A.; Voldman, J. Dielectrophoretic Traps for Single-Particle Patterning. *Biophys. J.* **2005**, *88*, 2193–2205.

31. Gielen, F.; Pereira, F.; deMello, A. J.; Edel, J. B. High-Resolution Local Imaging of Temperature in Dielectrophoretic Platforms. *Anal. Chem.* **2010**, *82*, 7509–7514.